CARS microscopy for the visualization of micrometer-sized iron oxide MRI contrast agents in living cells

Gianluca Rago,[1] Carolin M. Langer,[2] Christian Brackman,[3] James P.R. Day,[1] Katrin F. Domke,[1] Nathanael Raschzok,[2] Christian Schmidt,[4] Igor M. Sauer,[2] Annika Enejder,[3,5] Martina T. Mogl,[2,5] and Mischa Bonn[1,5,*]

[1]*FOM Institute AMOLF, Science Park 104, 1098XG Amsterdam, The Netherlands*
[2]*General, Visceral, and Transplantation Surgery and Regenerative Medicine, Charité-Campus Virchow, Universitätsmedizin Berlin, Augustenburger Platz 1, D-13353 Berlin, Germany*
[3]*Department of Chemical and Biological Engineering, Chalmers University of Technology, Kemivagen 4, Göteborg, Sweden*
[4]*Microparticles GmbH, Volmerstrasse 9A, D-12489 Berlin, German*
[5]*These authors contributed equally to the manuscript*
**bonn@amolf.nl*

Abstract: Micrometer-sized iron oxide particles (MPIOs) attract increasing interest as contrast agents for cellular tracking by clinical Magnetic Resonance Imaging (MRI). Despite the great potential of MPIOs for *in vivo* imaging of labeled cells, little is known on the intracellular localization of these particles following uptake due to the lack of techniques with the ability to monitor the particle uptake *in vivo* at single-cell level. Here, we show that coherent anti-Stokes Raman scattering (CARS) microscopy enables non-invasive, label-free imaging of MPIOs in living cells with sub-micron resolution in three dimensions. CARS allows simultaneous visualization of the cell framework and the MPIOs, where the particles can be readily distinguished from other cellular components of comparable dimensions, and localized inside the cell.

OCIS codes: (300.6230) Spectroscopy, coherent anti-Stokes Raman scattering; (180.6900) Three-dimensional microscopy; (020.4180) Multiphoton processes; (170.3880) Medical and biological imaging; (190.4380) Nonlinear optics, four-wave mixing; (160.4236) Nanomaterials

References and links

1. K. Krause, C. Schneider, K. H. Kuck, and K. Jaquet, "Review: Stem cell therapy in cardiovascular disorders," Cardiovasc. Ther. **28**(5), e101–e110 (2010).
2. T. Meyerrose, S. Olson, S. Pontow, S. Kalomoiris, Y. Jung, G. Annett, G. Bauer, and J. A. Nolta, "Mesenchymal stem cells for the sustained in vivo delivery of bioactive factors," Adv. Drug Deliv. Rev. **62**(12), 1167–1174 (2010).
3. J. Meyburg, A. M. Das, F. Hoerster, M. Lindner, H. Kriegbaum, G. Engelmann, J. Schmidt, M. Ott, A. Pettenazzo, T. Luecke, H. Bertram, G. F. Hoffmann, and A. Burlina, "One liver for four children: first clinical series of liver cell transplantation for severe neonatal urea cycle defects," Transplantation **87**(5), 636–641 (2009).
4. A. Dhawan, J. Puppi, R. D. Hughes, and R. R. Mitry, "Human hepatocyte transplantation: current experience and future challenges," Natl. Rev. **7**(5), 288–298 (2010).
5. R. A. Fisher and S. C. Strom, "Human hepatocyte transplantation: worldwide results," Transplantation **82**(4), 441–449 (2006).
6. S. Gupta, "Hepatocyte transplantation," J. Gastroenterol. Hepatol. **17**(s3 Suppl 3), S287–S293 (2002).
7. A. Dhawan, R. R. Mitry, and R. D. Hughes, "Hepatocyte transplantation for liver-based metabolic disorders," J. Inherit. Metab. Dis. **29**(2-3), 431–435 (2006).
8. Y. Kawashita, C. Guha, K. Yamanouchi, Y. Ito, Y. Kamohara, and T. Kanematsu, "Liver repopulation: a new concept of hepatocyte transplantation," Surg. Today **35**(9), 705–710 (2005).
9. E. Fitzpatrick, R. R. Mitry, and A. Dhawan, "Human hepatocyte transplantation: state of the art," J. Intern. Med. **266**(4), 339–357 (2009).
10. J. W. M. Bulte, "In vivo MRI cell tracking: clinical studies," AJR Am. J. Roentgenol. **193**(2), 314–325 (2009).
11. M. Modo, "Noninvasive imaging of transplanted cells," Curr. Opin. Organ Transplant. **13**(6), 654–658 (2008).

#150798 - $15.00 USD Received 8 Jul 2011; revised 25 Jul 2011; accepted 28 Jul 2011; published 29 Jul 2011

12. J. Puppi and M. Modo, "Use of magnetic resonance imaging contrast agents to detect transplanted liver cells," Top. Magn. Reson. Imaging **20**(2), 113–120 (2009).
13. A. Quaglia, S. C. Lehec, R. D. Hughes, R. R. Mitry, A. S. Knisely, S. Devereaux, J. Richards, M. Rela, N. D. Heaton, B. C. Portmann, and A. Dhawan, "Liver after hepatocyte transplantation for liver-based metabolic disorders in children," Cell Transplant. **17**(12), 1403–1414 (2008).
14. N. I. Bohnen, M. Charron, J. Reyes, W. Rubinstein, S. C. Strom, D. Swanson, and R. Towbin, "Use of indium-111-labeled hepatocytes to determine the biodistribution of transplanted hepatocytes through portal vein infusion," Clin. Nucl. Med. **25**(6), 447–450 (2000).
15. S. Koenig, P. Krause, A. S. A. Hosseini, C. Dullin, M. Rave-Fraenk, S. Kimmina, A. L. Entwistle, R. M. Hermann, C. F. Hess, H. Becker, and H. Christiansen, "Noninvasive imaging of liver repopulation following hepatocyte transplantation," Cell Transplant. **18**(1), 69–78 (2009).
16. W. M. Leevy, S. T. Gammon, J. R. Johnson, A. J. Lampkins, H. Jiang, M. Marquez, D. Piwnica-Worms, M. A. Suckow, and B. D. Smith, "Noninvasive optical imaging of staphylococcus aureus bacterial infection in living mice using a Bis-dipicolylamine-Zinc(II) affinity group conjugated to a near-infrared fluorophore," Bioconjug. Chem. **19**(3), 686–692 (2008).
17. P. F. Renshaw, C. S. Owen, A. E. Evans, and J. S. Leigh, Jr., "Immunospecific NMR contrast agents," Magn. Reson. Imaging **4**(4), 351–357 (1986).
18. S. J. Dodd, M. Williams, J. P. Suhan, D. S. Williams, A. P. Koretsky, and C. Ho, "Detection of single mammalian cells by high-resolution magnetic resonance imaging," Biophys. J. **76**(1), 103–109 (1999).
19. E. M. Shapiro, S. Skrtic, K. Sharer, J. M. Hill, C. E. Dunbar, and A. P. Koretsky, "MRI detection of single particles for cellular imaging," Proc. Natl. Acad. Sci. U.S.A. **101**(30), 10901–10906 (2004).
20. A. S. Arbab and J. A. Frank, "Cellular MRI and its role in stem cell therapy," Regen. Med. **3**(2), 199–215 (2008).
21. E. M. Shapiro, K. Sharer, S. Skrtic, and A. P. Koretsky, "In vivo detection of single cells by MRI," Magn. Reson. Med. **55**(2), 242–249 (2006).
22. J. Grimm, M. F. Kircher, and R. Weissleder, "Cell tracking," Radiologe **47**(1), 25–33 (2007).
23. S. G. Crich, L. Biancone, V. Cantaluppi, D. Duò, G. Esposito, S. Russo, G. Camussi, and S. Aime, "Improved route for the visualization of stem cells labeled with a Gd-/Eu-chelate as dual (MRI and fluorescence) agent," Magn. Reson. Med. **51**(5), 938–944 (2004).
24. H. E. Daldrup-Link, M. Rudelius, S. Metz, G. Piontek, B. Pichler, M. Settles, U. Heinzmann, J. Schlegel, R. A. J. Oostendorp, and E. J. Rummeny, "Cell tracking with gadophrin-2: a bifunctional contrast agent for MR imaging, optical imaging, and fluorescence microscopy," Eur. J. Nucl. Med. Mol. Imaging **31**(9), 1312–1321 (2004).
25. T. D. Henning, O. Saborowski, D. Golovko, S. Boddington, J. S. Bauer, Y. J. Fu, R. Meier, H. Pietsch, B. Sennino, D. M. McDonald, and H. E. Daldrup-Link, "Cell labeling with the positive MR contrast agent Gadofluorine M," Eur. Radiol. **17**(5), 1226–1234 (2007).
26. M. Srinivas, P. A. Morel, L. A. Ernst, D. H. Laidlaw, and E. T. Ahrens, "Fluorine-19 MRI for visualization and quantification of cell migration in a diabetes model," Magn. Reson. Med. **58**(4), 725–734 (2007).
27. N. Himes, J. Y. Min, R. Lee, C. Brown, J. Shea, X. L. Huang, Y. F. Xiao, J. P. Morgan, D. Burstein, and P. Oettgen, "In vivo MRI of embryonic stem cells in a mouse model of myocardial infarction," Magn. Reson. Med. **52**(5), 1214–1219 (2004).
28. J. Pinkernelle, U. Teichgräber, F. Neumann, L. Lehmkuhl, J. Ricke, R. Scholz, A. Jordan, and H. Bruhn, "Imaging of single human carcinoma cells in vitro using a clinical whole-body magnetic resonance scanner at 3.0 T," Magn. Reson. Med. **53**(5), 1187–1192 (2005).
29. J. Lodhia, G. Mandarano, Nj. Ferris, P. Eu, and S. F. Cowell, "Development and use of iron oxide nanoparticles (Part 1): Synthesis of iron oxide nanoparticles for MRI," Biomed Imaging Intervent. J. **6**(2), e12 (2010).
30. M. H. Morgul, N. Raschzok, R. Schwartlander, F. W. Vondran, R. Michel, L. Stelter, J. Pinkernelle, A. Jordan, U. Teichgraber, and I. M. Sauer, "Tracking of primary human hepatocytes with clinical MRI: initial results with Tat-peptide modified superparamagnetic iron oxide particles," Int. J. Artif. Organs **31**(3), 252–257 (2008).
31. W. Liu and J. A. Frank, "Detection and quantification of magnetically labeled cells by cellular MRI," Eur. J. Radiol. **70**(2), 258–264 (2009).
32. I. J. M. de Vries, W. J. Lesterhuis, J. O. Barentsz, P. Verdijk, J. H. van Krieken, O. C. Boerman, W. J. G. Oyen, J. J. Bonenkamp, J. B. Boezeman, G. J. Adema, J. W. M. Bulte, T. W. J. Scheenen, C. J. A. Punt, A. Heerschap, and C. G. Figdor, "Magnetic resonance tracking of dendritic cells in melanoma patients for monitoring of cellular therapy," Nat. Biotechnol. **23**(11), 1407–1413 (2005).
33. Z. Medarova, P. Vallabhajosyula, A. Tena, N. Evgenov, P. Pantazopoulos, V. Tchipashvili, G. Weir, D. Sachs, and A. Moore, "In vivo imaging of autologous islet grafts in the liver and under the kidney capsule in non-human primates," Transplantation **87**(11), 1659–1666 (2009).
34. K. A. Hinds, J. M. Hill, E. M. Shapiro, M. O. Laukkanen, A. C. Silva, C. A. Combs, T. R. Varney, R. S. Balaban, A. P. Koretsky, and C. E. Dunbar, "Highly efficient endosomal labeling of progenitor and stem cells with large magnetic particles allows magnetic resonance imaging of single cells," Blood **102**(3), 867–872 (2003).
35. E. M. Shapiro, S. Skrtic, and A. P. Koretsky, "Sizing it up: cellular MRI using micron-sized iron oxide particles," Magn. Reson. Med. **53**(2), 329–338 (2005).
36. N. Raschzok, M. H. Morgul, J. Pinkernelle, F. W. R. Vondran, N. Billecke, N. N. Kammer, G. Pless, M. K. Adonopoulou, C. Leist, L. Stelter, U. Teichgraber, R. Schwartlander, and I. M. Sauer, "Imaging of primary human hepatocytes performed with micron-sized iron oxide particles and clinical magnetic resonance tomography," J. Cell. Mol. Med. **12**(4), 1384–1394 (2008).

#150798 - $15.00 USD Received 8 Jul 2011; revised 25 Jul 2011; accepted 28 Jul 2011; published 29 Jul 2011

37. M. Muller, *Introduction to confocal fluorescence microscopy* (Shaker Publishing, Maastricht, 2002).
38. S. Schwarz, F. Fernandes, L. Sanroman, M. Hodenius, C. Lang, U. Himmelreich, T. Schmitz-Rode, D. Schueler, M. Hoehn, M. Zenke, and T. Hieronymus, "Synthetic and biogenic magnetite nanoparticles for tracking of stem cells and dendritic cells," J. Magn. Magn. Mater. **321**(10), 1533–1538 (2009).
39. A. M. Schrand, J. J. Schlager, L. M. Dai, and S. M. Hussain, "Preparation of cells for assessing ultrastructural localization of nanoparticles with transmission electron microscopy," Nat. Protoc. **5**(4), 744–757 (2010).
40. J. X. Cheng, A. Volkmer, and X. S. Xie, "Theoretical and experimental characterization of coherent anti-Stokes Raman scattering microscopy," J. Opt. Soc. Am. B **19**(6), 1363–1375 (2002).
41. J. P. R. Day, K. F. Domke, G. Rago, H. Kano, H. O. Hamaguchi, E. M. Vartiainen, and M. Bonn, "Quantitative Coherent Anti-Stokes Raman Scattering (CARS) Microscopy," J. Phys. Chem. B **115**(24), 7713–7725 (2011).
42. A. Enejder, C. Brackmann, and F. Svedberg, "Coherent Anti-Stokes Raman Scattering Microscopy of Cellular Lipid Storage," IEEE J. Sel. Top. Quantum Electron. **16**(3), 506–515 (2010).
43. T. Hashimoto, T. Yamada, and T. Yoko, "Third-order nonlinear optical properties of sol-gel derived alpha-Fe2O3, gamma-Fe2O3, and Fe3O4 thin films," J. Appl. Phys. **80**(6), 3184–3190 (1996).
44. H. S. Nalwa and S. Miyata, *Nonlinear Optics of Organic Molecules and Polymers* (CRC Press, Boca Raton, FL, 1997).
45. T. Hellerer, C. Axäng, C. Brackmann, P. Hillertz, M. Pilon, and A. Enejder, "Monitoring of lipid storage in *Caenorhabditis elegans* using coherent anti-Stokes Raman scattering (CARS) microscopy," Proc. Natl. Acad. Sci. U.S.A. **104**(37), 14658–14663 (2007).
46. J. P. R. Day, G. Rago, K. F. Domke, K. P. Velikov, and M. Bonn, "Label-free imaging of lipophilic bioactive molecules during lipid digestion by multiplex coherent anti-Stokes Raman scattering microspectroscopy," J. Am. Chem. Soc. **132**(24), 8433–8439 (2010).
47. M. Okuno, H. Kano, P. Leproux, V. Couderc, J. P. R. Day, M. Bonn, and H. O. Hamaguchi, "Quantitative CARS molecular fingerprinting of single living cells with the use of the maximum entropy method," Angew. Chem. Int. Ed. Engl. **49**(38), 6773–6777 (2010).
48. G. Rago, B. Bauer, F. Svedberg, L. Gunnarsson, M. B. Ericson, M. Bonn, and A. Enejder, "Uptake of gold nanoparticles in healthy and tumor cells visualized by nonlinear optical microscopy," J. Phys. Chem. B **115**(17), 5008–5016 (2011).
49. J. Moger, B. D. Johnston, and C. R. Tyler, "Imaging metal oxide nanoparticles in biological structures with CARS microscopy," Opt. Express **16**(5), 3408–3419 (2008).
50. Y. Zheng, G. Holtom, and S. D. Colson, "Multichannel multiphoton imaging of metal oxides nanoparticles in biological system," Proc. SPIE **5323**, 390–399 (2004).
51. Y. Wang, C.-Y. Lin, A. Nikolaenko, V. Raghunathan, and E. O. Potma, "Four-wave mixing microscopy of nanostructures," Adv. Opt. Photonics **3**(1), 1–52 (2011).
52. J. Burris and T. J. McIlrath, "Theoretical study relating the two-photon absorption cross section to the susceptibility controlling four-wave mixing," J. Opt. Soc. Am. B **2**(8), 1313–1317 (1985).
53. E. W. Van Stryland, M. A. Woodall, H. Vanherzeele, and M. J. Soileau, "Energy band-gap dependence of two-photon absorption," Opt. Lett. **10**(10), 490–492 (1985).
54. J. X. Cheng and X. S. Xie, "Coherent anti-Stokes Raman scattering microscopy: Instrumentation, theory, and applications," J. Phys. Chem. B **108**(3), 827–840 (2004).
55. X. L. Nan, J. X. Cheng, and X. S. Xie, "Vibrational imaging of lipid droplets in live fibroblast cells with coherent anti-Stokes Raman scattering microscopy," J. Lipid Res. **44**(11), 2202–2208 (2003).
56. D. Gachet, F. Billard, N. Sandeau, and H. Rigneault, "Coherent anti-Stokes Raman scattering (CARS) microscopy imaging at interfaces: evidence of interference effects," Opt. Express **15**(16), 10408–10420 (2007).

1. Introduction

Cell transplantation using, e.g., stem cells, progenitor cells and adult cell lines constitutes a promising approach for treatment of several human diseases [1,2], and has already been tested for clinical treatment of cardiovascular, neurological, and metabolic disorders [1,3–6]. The advantages compared to whole organ transplantation are many: the less invasive treatment, the use of cryopreserved cells, and the possibility that an organ from a single donor can be used for treatment of multiple patients [7–9]. Substantial effort has been devoted to the development of techniques to image individual cells in live organisms, as monitoring cell transplantation is crucial for the success of the therapy. Such imaging allows the detection of the early stages of cell homing, tracking cell migration, and the visualization of complications such as microembolization of transplanted cells [10–13].

The outcome of cell transplantation in clinical trials has been investigated via biopsies from the target organ, using visualization by radioisotope imaging [14]. This approach has serious limitations, however: it is associated with a risk for the patient due to the invasive procedure and constrained by the fact that only a limited part of the organ can be investigated, and only at limited numbers of moments in time. Alternatively, optical labels have been tested

#150798 - $15.00 USD Received 8 Jul 2011; revised 25 Jul 2011; accepted 28 Jul 2011; published 29 Jul 2011

in the visualization with Near Infrared Fluorescence (NIRF) Optical Imaging of the development of transplanted cells in vivo in a preclinical rat-model [15]. A major drawback of this method is that NIRF-dyes are only detectable up to a tissue thickness of about 2 to 3 cm in vivo [16] and that the NIRF-dye must present antigen specificity. The discovery of immunospecific NMR contrast agents [17] has enabled magnetic resonance imaging (MRI) as a suitable tool for non-invasive tracking of transplanted labeled cells. The technique was first employed for imaging single cells *in vitro* [18,19] and has since been extended to cells *in vivo* [20,21]. MRI is currently the most common imaging technique for tracking *in vivo* labeled cells owing to its high resolution, and enhanced tissue contrast [22]. This technology further benefits from its widespread availability in clinical environments. The progress of the technique *in vivo* relies primarily on the choice of cell labels that are easily internalized by cells and can be readily visualized by MRI. However, to date it has remained challenging to fully elucidate the cellular uptake mechanism of these particles. In this study, we present a combination of resonant and nonresonant Coherent anti-Stokes Raman Scattering (CARS) microscopy as a useful tool for the visualization of MRI labels in living cells.

Paramagnetic Gadolinium (Gd) chelates are commonly used as T_1 contrast agents, although their low permeability through the cell membrane requires high concentrations combined with long incubation times for efficient internalization, and the detectability of labeled cells was found to be insufficient for clinical applications [23]. Gd-based metalloporphirins, e.g. gadophrin-2 [24], and amphiphilic chelates, e.g. Gadofluorine M [25], are readily internalized by cells, but high concentrations are still required for MRI detection. Perfluorocarbons have also been investigated as cell labels [26] with the advantage that ^{19}F MRI provides background-free imaging of the cells. Regrettably, they exhibited inadequate signal levels. Superparamagnetic iron oxide (SPIO) nanoparticles have successfully been used as T_2 and T_2* contrast agents and exhibit higher contrast compared to normal paramagnetic particles [27,28]. SPIOs possess very high molar relaxivity, giving rise to contrast that well exceeds the physical dimensions of the particles *in vitro*. In addition, their magnetic properties can be tailored by modifying the particle size and aspect ratio [29]. These particles are negative contrast agents, appearing as pronounced hypointense regions in MR images. The major drawback of nanometer-sized SPIOs as labels is that a significant number of particles is required within a voxel for efficient detection. Thus, the dilution of the label as a result of cell division inevitably reduces the local concentration below the detection limit after a few life cycles of the cells [19]. SPIOs have primarily been used for detecting single cells *in vitro* [30] (For a general review on primary human hepatocytes see [31]), but also *in vivo* by clinical MR equipment [32]. Clinical MRI was found to be limited by the relatively low field strength and resolution compared to what was shown in experimental studies [33]. The conclusion from these efforts is that larger particles creating a greater magnetic moment within the cells would be desirable for efficient detection of labeled cells under clinical conditions.

Labeling with micrometer-sized iron oxide particles (MPIO) with higher magnetic relaxation compared to SPIOs constitutes a promising approach towards optimized imaging capabilities. It has been shown that MPIOs exhibit increased relaxation compared to nanometer-sized particles with the same total iron content per unit sample volume [34]. MPIOs can be easily internalized by several types of cells and allow for labeling capacity up to hundreds of picograms of iron per cell without affecting cellular viability [35]. For instance, primary human hepatocytes can be labeled with MPIOs without negative effects on cellular integrity or metabolic activity [36]. MPIOs have been used for MR imaging of cells both *in vitro* [19,34] and *in vivo* [21], and it has been shown that even single MPIO can be detected by MRI at a resolution of 100 μm [35]. Single particle sensitivity implies that MRI detection is not compromised by cell division due to dilution of the label.

Efficient uptake of the label is a crucial step for cell tracking, and an understanding of the underlying mechanisms is crucial for optimizing the labeling process. Also, unambiguous determination of the average number of MPIOs taken up per cell is crucial to evaluate MRI

#150798 - $15.00 USD Received 8 Jul 2011; revised 25 Jul 2011; accepted 28 Jul 2011; published 29 Jul 2011

results and adapt the labeling protocol. Much research is expected to be dedicated to structural and functional modifications of the particles in order to achieve both better MRI contrast and specific cellular uptake. Any imaging technique that would support these studies must fulfill quite stringent requirements. The technique must be firstly non-invasive in order not to affect the health of the cells, and label-free in order to study the interaction between the cell and the MPIOs under realistic and biologically relevant conditions: all invasive forms of sample preparation such as staining and sectioning are undesirable; finally, it must offer sub-cellular resolution, three-dimensional imaging capabilities and contrast from both MPIOs and cells. The ability of present technology to monitor intracellular localization of MPIO is still rudimentary due to the difficulties of colocalizing the particles with cellular components without the use of labels.

Conventional brightfield microscopy based on light transmission is the fastest and least invasive approach for visualizing the particles *in vitro* [35,36], but unfortunately provides neither chemical selectivity nor sufficient axial resolution. In this technique, MPIOs are identified from their shape, with the risk of false positive identifications from large lipid droplets or other circular organelles in the cell. Due to the limited axial resolution, it is challenging to retrieve information on the localization of the particles relative to intracellular features from this approach. Knowledge of the location of particles is especially important relative to the external cellular membrane; brightfield microscopy is not able to differentiate between a microparticle sitting outside the cell from one that has been internalized but still located in proximity to the membrane. Multi-channel confocal and two-photon fluorescence microscopies provide a viable alternative, allowing for visualization of fluorescently labeled components of the cells and labeled particles [21]. For instance, one among many possible options is double staining for cytoplasmic proteins and nucleus, combined with additional staining of MPIOs [36]. While multi-channel fluorescence microscopy overcomes the spatial resolution issues of light microscopy [37], the approach is limited to the visualization of the particles relative to one or a few intracellular components, which in addition are studied under artificial conditions in the presence of multiple fluorescent marker molecules. In systems so critically dependent on local chemical and physical properties as the nano-bio interface, the presence of additional labels is undesirable as it can perturb the nature and dynamics of biological and physical interactions. Transmission electron microscopy (TEM) has also been used to visualize the uptake of MPIOs [38]. TEM has the ability to resolve both particles and cellular components on nanometer length scales. However, significant limitations of this approach may be noted, including the time-consuming and highly invasive sample preparation associated with potential artifacts [39]; cell fixation, resin embedding and slicing of the cells. This technique also precludes studies of the temporal characteristics of the particle integration process.

As we will show here, the combination of resonant and non-resonant CARS microscopy represents a useful label-free approach to the visualization of MPIOs in living cells. The particles are readily distinguished from micrometer sized cellular features such as cytoplasmatic lipid bodies based on their high density of electrons. The approach is shown to provide accurate localization of the particles with respect with the cell body. Due to the multi-photon nature of the CARS process, high spatial resolution is ensured both laterally (~300 nm) and axially (~1 μm) with three-dimensional imaging capabilities [40]. We refer here to CARS as a special case of Four Wave Mixing (FWM) where three incident fields, two with degenerate frequency ω_1 (pump/probe beam), and a third with frequency ω_2 (Stokes beam), interact through the third-order susceptibility of the probed material, generating a blue shifted fourth field at the anti-Stokes frequency $\omega_{AS} = 2\omega_1 - \omega_2$.

The intensity of the detected CARS field is proportional to the induced third order polarization $P^{(3)}$, which in turn depends on the intensity of the incident fields and on the squared modulus of the third order susceptibility $\chi^{(3)}$ at the anti-Stokes frequency:

#150798 - $15.00 USD Received 8 Jul 2011; revised 25 Jul 2011; accepted 28 Jul 2011; published 29 Jul 2011

$$I_{CARS}(\omega_{AS}) \propto \left|P^{(3)}(\omega_{AS})\right|^2 = \left|E_1\right|^4 \left|E_2\right|^2 \left|\chi^{(3)}(\omega_{AS})\right|^2 \quad (1)$$

The general expression of the third order molecular susceptibility

$$\chi^{(3)}(\omega_{AS}) = \chi_R^{(3)}(\omega_{AS}) + \chi_{NR}^{(3)} \quad (2)$$

contains a resonant (*R*) and a non-resonant (*NR*) term. The non-resonant contribution arises from the intrinsic electronic polarizability of the material (see energy diagram in Fig. 1a-b). For the wavelengths and limited spectral window used here, the non-resonant term is real, nonzero and frequency-invariant. The resonant term can be written as [41]

$$\chi_R^{(3)}(\omega_{AS}) = \sum_j \frac{A_j}{\Omega_j - (\omega_1 - \omega_2) - i\Gamma_j} \quad (3)$$

where A_j, Ω_j and Γ_j are the amplitude, spectral position and Raman linewidth of the *j*-th vibrational resonance respectively. The resonant component is thus enhanced when the frequency difference of the incoming fields is in resonance with a vibrational eigenfrequency of a specific molecular bond, as illustrated in the energy diagram in Fig. 1c.

The bioorganic molecules of the cell and the inorganic oxide of the MPIOs can be visualized by tuning the frequency difference of the fields to be on- ($\omega_1 - \omega_2 = 2845$ cm^{-1}) and off-resonance ($\omega_1 - \omega_2 = 3000$ cm^{-1}) with the symmetric stretch vibration of the CH_2 groups (see spectrum in Fig. 1d). On-resonant excitation yields an enhanced CARS signal from lipid-rich components of the cells [42], accompanied by a strong non-resonant electronic signal from the MPIOs due to the high electron density of the iron oxide. Off-resonant excitation provides a weak non-resonant signal from the cells, but the strong non-resonant electronic signal from the MPIOs remains. The difference in the magnitude of the non-resonant signals arises from the large difference of the electronic susceptibility of iron oxide (4 x 10^{-10} esu [43]) compared to that of biological matter (typically 10^{-13} esu [44]). It is important to underline that due to the large dimensions of MPIOs, the particles have the same physical properties of bulk iron oxide. Owing to the very small bandgap of this material (E_{gap} = 0.14

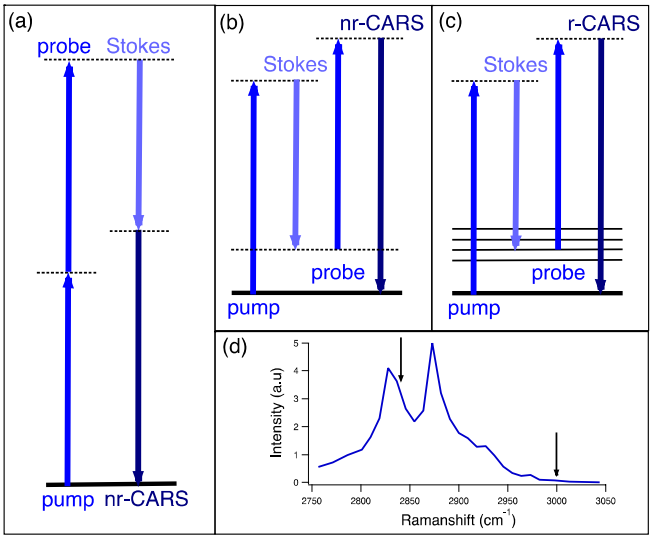

Fig. 1. Energy schemes of the nonresonant (a and b) and resonant CARS (c) process. (d) Normalized CARS spectrum of tripalmitin; the arrows at 2845 cm^{-1} and 3000 cm^{-1} indicate the typical response of biological matter at the frequencies used for on- and off-resonance CARS measurements.

#150798 - $15.00 USD Received 8 Jul 2011; revised 25 Jul 2011; accepted 28 Jul 2011; published 29 Jul 2011

eV, corresponding to a band edge absorption of 8.8 μm), the optical response in the visible and near-IR wavelength range is largely frequency independent. The results obtained here for our CARS set-up with its specific combination of wavelengths should therefore be generally applicable to other CARS setups as well, as this wavelength range includes the excitation wavelengths of the beams normally employed in CARS experiments. As the contrast is derived from molecular properties, no additional staining of the sample is required for imaging [45,46]. Additionally, the use of excitation beams in the near-infrared is particularly suitable for imaging biological samples as the absorption cross-section of water is low in this region [47].

CARS has previously been employed to visualize gold nanoparticles in cells [48], as well as wide bandgap semiconductor oxide nanoparticles in biological systems [49,50]. In the latter works, the energy of bandgap absorption of a material is matched by the second harmonic of one of the excitation beams, resulting in a third term that contributes to the molecular susceptibility arising from two-photon electronic resonance in Eq. (2). The response of these particles is enhanced and gives rise to very high signals that allow to readily distinguish the particles from their environment [51]. The enhancement is nevertheless limited to the coupling of the two photons to the electronic states in the vicinity of the energy gap, where the effects of excitons are expected to be larger [52,53]. This effect is negligible in magnetite as, contrary to other oxides, this material has a small bandgap of 0.14 eV.

Two consecutive CARS measurements, on and off-resonance, are hence necessary to distinguish MPIOs from the biological components. This apparent drawback turns out to be an advantage as the overlay of on- and off-resonance CARS measurements of the same region provides unambiguous determination of the location of each MPIO within the cell, and intrinsically discriminates between them and micrometer-size lipid structures that may easily be confused in brightfield images of the cells.

2. Materials and methods

2.1. CARS microscope

The microscopy setup is based on a picosecond laser system generating two synchronized beams collinearly aligned into an inverted microscope (Eclipse TE-2000, Nikon, Tokyo, Japan) via a beam scanning unit (C1, Nikon). A fraction of the fundamental output of a Nd:Van laser (Picotrain, HighQ Lasers GmbH, Hohenems, Austria) at 1064 nm is directly coupled into the microscope as the Stokes beam. The remaining fraction is frequency-doubled (532 nm) and used to synchronously pump an Optical Parametric Oscillator (Emerald OPO, APE GmbH, Berlin, Germany). The OPO provides a wavelength tunable output beam, in this work set either to 817 nm or 807 nm in order to form a beating excitation field with the Stokes beam at the frequencies of 2845 cm^{-1} and 3000 cm^{-1} respectively. The Raman shift of 2845 cm^{-1} corresponds to the symmetric stretch vibration of the CH_2 group in the acyl chain of lipids, whereas the Raman shift of 3000 cm^{-1} corresponds to a spectral region where lipid structures present a low response. This can be seen in the CARS spectrum in Fig. 1d collected from a tripalmitin crystal as an example of a typical saturated fatty acid compound, where the intensity of the response at the above frequencies is marked with arrows. CARS measurements at 2845 cm^{-1} and 3000 cm^{-1} are in the following text referred to as *on-resonance* and *off-resonance* respectively. The laser beams were focused on the sample with an oil immersion objective (Plan Fluor 40× , NA 1.30, Nikon), resulting in a power of 10 mW for each of the beams at the sample position. Prior to the imaging measurements, we tested the optimal experimental conditions and found that this laser power combined with an imaging time of 20 s per image (256x256 pixels) provided optimal results in that both the cells and the particles are clearly visible in the images without compromising the viability of the cells. The CARS signal was collected by an aspherical lens (NA 0.68) in the forward direction and detected by a single-photon counting photomultiplier tube (PMC-100, Hamamatsu) connected

#150798 - $15.00 USD Received 8 Jul 2011; revised 25 Jul 2011; accepted 28 Jul 2011; published 29 Jul 2011

to a time-correlated single-photon counting unit (SPCM-830, Becker and Hickl). Bandpass filters in front of the detector suppressed the radiation at the laser wavelengths and transmitted the generated CARS signal. A detailed outline of the setup is given by Enejder *et al.* [42]. Three-dimensional imaging was achieved by scanning a sequence of horizontal planes at different vertical positions by translating the objective with a motorized stage. Samples were first imaged in brightfield mode and the regions of interest, typically covering an area of 30x30 μm^2 (256x256 pixels), were then measured by CARS, and eventually imaged at different vertical positions with 1 micron spacing. *On-resonance* and *off-resonance* images of the same region of the sample were collected consecutively by changing the wavelength of the OPO and allowing for ~1 minute stabilization of the laser system. The output of the OPO was optimized for the *on-resonance* measurement, and the same settings were kept in the *off-resonance* measurement resulting in a small loss of power. The total acquisition time for each layer was 20 s at each wavelength. The tripalmitin CARS spectrum of Fig. 1d was measured under similar experimental conditions as the cell studies, images were collected on a tripalmitin crystal with the OPO tuned to wavelengths in the range 802-823 nm, thus probing frequencies between 2750 and 3050 cm^{-1}. For each tripalmitin image a corresponding reference image of the sample cover glass was measured for CARS signal normalization, and the spectrum shows the average normalized crystal signal versus probed frequency.

2.2. Micron-sized iron oxide particles

MPIOs were obtained from Microparticles GmbH (Berlin, Germany). The average diameter of each microparticle is 1.18 +/– 0.08 µm. Microspheres consist of a silica based matrix with homogeneously incorporated iron oxide nanoparticles (40 vol-%). A hydrophilic polymer layer surrounds the core to prevent leaching of iron species. Additionally streptavidin functionality was introduced to the surface of the particles via 1-ethyl-3-(3-dimethylaniminopropryl) carbodiimide (EDC)-coupling. The particles have a narrow size distribution, are superparamagnetic and show a very good colloidal stability in phosphate buffered saline (PBS) solution. The concentration of the particles in 1% w/v aqueous stock suspension was 7.088 x 10^9 particles per mL, resulting in an iron content of approximately 2.88 mg/mL. Subsamples from the stock solution were dissolved with PBS to suspension concentration of 10^7 particles/mL and stored at 4°C under sterile conditions until cell incubation.

2.3. Cell cultures and incubation with MPIOs

Cryopreserved HuH7 cells, from a well-differentiated human hepatoma cell line, were purchased from JCRB Cell Bank (Osaka, Japan). Cells were thawed in a water bath and cultured in 25mm^2 culture flasks (Sarstedt, Nürnberg, Germany) using Dulbecco's minimal essential medium (Biochrom AG, Berlin, Germany), supplemented with 10% fetal bovine serum (FBS), 1% L- Alanyl- L- Glutamine (200mM), 1% sodium pyruvat (100mM) and 1% penicillin-streptomycin at 37°C with 5% CO_2 atmosphere and 100% humidity. The cultures were passaged until a confluent layer was formed. Cells were washed with PBS and then released from the flask by incubating with 0,05% trypsin/0,02% EDTA for 4 min. at 37°C. Growth medium at 4 °C with 10% FBS was added to the cell suspension in order to stop the enzyme activity. A representative number of HuH7 cells were stained with Tryphan blue and counted in a hemocytometer. 100,000 living cells were seeded on sterile WillCo petri dishes (series GWSt-5030) with a 0.17 mm thick glass bottom and allowed to attach for 1 h at 37°C in 5% CO_2. Cells were washed and fresh medium was supplied.

Particles were gently resuspended prior to incubation, and 1mL particle solution was added to 1 mL growth medium in the dish. The MPIO amounted to100 beads per cell. The cells were incubated for 4h at 37°C in 5% CO_2. As controls, native cells were treated identically, but without particles. To remove free particles after incubation, the cells were extensively washed with PBS. The slides with the living cells were immediately transferred to

#150798 - $15.00 USD Received 8 Jul 2011; revised 25 Jul 2011; accepted 28 Jul 2011; published 29 Jul 2011

the microscope for imaging. After the procedure it was visually confirmed that the cells were still intact. The time span between seeding the cells, particle incubation and CARS measurements lasted no longer than 48h.

3. Results and discussion

3.1. Imaging of dried MPIO solution

To ascertain selective imaging of MPIOs in cells, *on-resonance* and *off-resonance* images were first collected on a reference sample of pure MPIOs. A droplet of solution containing 10^8 particles/mL of MPIOs was left to dry for one hour on a conventional microscope cover slip before imaging with both brightfield and CARS microscopy.

Figure 1a shows a brightfield microscopy image of a region of the sample where three MPIOs can be identified. The same region was consecutively imaged with CARS, first with the pump and Stokes beams tuned to match the excitation energy of CH_2 bonds (*on-resonance* measurement), presented in Fig. 2b, and then with the beams tuned away from the resonance (*off-resonance* measurement), presented in Fig. 2c. Each of the three images covers an area of 10×30 μm^2.

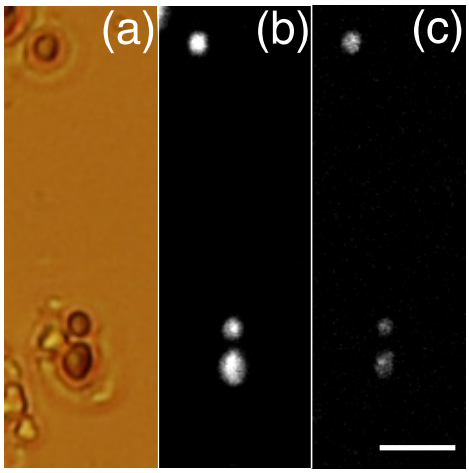

Fig. 2. Brightfield microscopy (a), on-resonance (b) and off-resonance (c) CARS images of a 10×30 μm^2 –sized region of dried solution of MPIOs. Scale bar 5 μm. The normalized intensity of the signal measured from MPIOs on- and off resonance is identical within the variations that result from frequency tuning.

By overlaying the *on-* and *off-resonance* CARS images in Figs. 2b and 2c, perfect colocalization of the features is obtained. Due to the lack of resonant signal together with a strong non-resonant contribution, the three particles are clearly visible in both CARS images, indicating that the optical contrast is not of vibrational origin but is related to a purely electronic response. Hence, for the measurements reported in Figs. 2b and 2c, one would expect the same signal strength. The decrease in signal intensity in *off-resonance* mode (Fig. 2c) is not of physical origin but can be ascribed to the experimental procedure; the set-up is initially optimized for the *on-resonance* measurements. To minimize the time between the two consecutive measurements no additional optimization was performed after tuning the instrument to *off-resonance* excitation wavelength, resulting in a power loss in the output of the OPO. This can be confirmed by observing that also the reference signal measured from the glass cover slip is reduced accordingly between the two measurements. Within the signal fluctuation and variations resulting from frequency tuning, the signal intensities measured *on-* and *off-resonance* are identical after normalization by the reference response measured in glass.

#150798 - $15.00 USD Received 8 Jul 2011; revised 25 Jul 2011; accepted 28 Jul 2011; published 29 Jul 2011

We conclude from the CARS images presented in Fig. 2 that the contrast, or signal to background ratio, is in both cases (*on-* and *off-resonance*) large enough to enable precise identification of the particles. Since the dimensions of the particles are larger than the excitation wavelengths, detection of the CARS signal occurs here in forward direction. Extending this imaging approach to nanometer sized magnetite particles would instead be likely to benefit from epi-detection of the signal, as backward collection geometry is preferable for the visualization of objects with lateral dimensions comparable or smaller than the excitation wavelength [54]. The intensity profile taken along the diameter of any of the three round shapes fits well with the response expected from a 1.2 μm sized particle (data not shown).

3.2. Imaging of HuH7 cells in absence of MPIOs

Before interpreting the images of HuH7 cells incubated with the microparticles, the typical CARS response of these cells was characterized and compared with conventional brightfield microscopy. Figure 3a shows a brightfield microscopy image of a single cell. The cell is flat and spread over a large area, with peripheral terminals visible at its edge, giving rise to additional contact between the cell and the glass support. The nucleus is visible in the center of the image. Its irregular shape is typical for tumor cell lines. Cellular features have low contrast, except for the many anonymous circular features with diameters of ~1 μm that surround the nucleus. From this image it is clear that MPIOs will be difficult to distinguish from other intracellular features by conventional brightfield microscopy. The *on-resonance* CARS response of the same area (30×30 μm^2), imaged at an axial position ~2 μm above the glass surface is shown in Fig. 3b. This image appears similar to the brightfield microscopy, but it is important to underline that the CARS image is not merely a map of density or light transmission variations, but contains local chemical information as the intensity of the response is correlated to the concentration of CH_2 bonds within the focal volume. The peripheral terminals are not as clearly visible in the CARS image, indicating that these are located at an axial position closer to the supporting glass. Several features with particularly high intensities appear, leading us to conclude that these are lipid bodies, known to exhibit large CARS signals in this frequency range. The number of droplets is significantly smaller than the number of micron-sized features in the brightfield image, which illustrates an important limitation of conventional microscopy; the brightfield image is a projection of the entire cell volume showing all cellular features irrespective of their chemical composition or axial position. The CARS image instead gives a chemically specific picture of the distribution of lipids within a 1-μm thick focal plane. These lipids are present both in dense lipid droplets and in the cytoplasm (see Fig. 3b). The *on-resonance* CARS signal is particularly helpful to identify the outline of the cell and the nucleus. The nucleus can be identified in an indirect way as the round region in the center of the cell where the high intensity features indicating the presence of lipid-rich aggregates are not present.. The nucleolus is barely visible, indicating that it is located at a different axial position (compare Fig. 4a). These imaging capabilities of CARS microscopy are of particular importance in order to determine whether the MPIOs actually have entered the cells, and if so, to distinguish the particles from natural intracellular components of similar size. The *off-resonance* CARS image of the area is presented in Fig. 3c. The image appears as a negative of the *on-resonance* image, with intensities lower or similar to that of the medium surrounding the cell. The appearance of the lipid bodies as dark regions in Fig. 3c – i.e. giving a lower CARS signal *off-resonance* than both the water surrounding the cell and the aqueous solution inside the cell – can be traced to the relatively large signal from the water at the *off-resonance* frequency (3000 cm^{-1}) that arises from the flank of the broad OH stretch, and hence presents low but non-zero CARS response. In the lipid bodies, where no (or very little) water is present, the CARS response is truly *off-resonance*; in both water environments the tail of the water response gives rise to small, but finite signal. It is particularly remarkable how this effect makes the edges of cell

#150798 - $15.00 USD Received 8 Jul 2011; revised 25 Jul 2011; accepted 28 Jul 2011; published 29 Jul 2011

and nucleus well defined and readily visible in comparison with the background. This negative-like response is useful as it still gives an indication on the localization of cellular components in the *off-resonance* measurements where primarily MPIOs are detected. It is important to note that the lipid bodies in the cytoplasm are likely to slightly change their position over time, but in most cases the time between different CARS images is short enough so that the lipid bodies can be tracked in time.

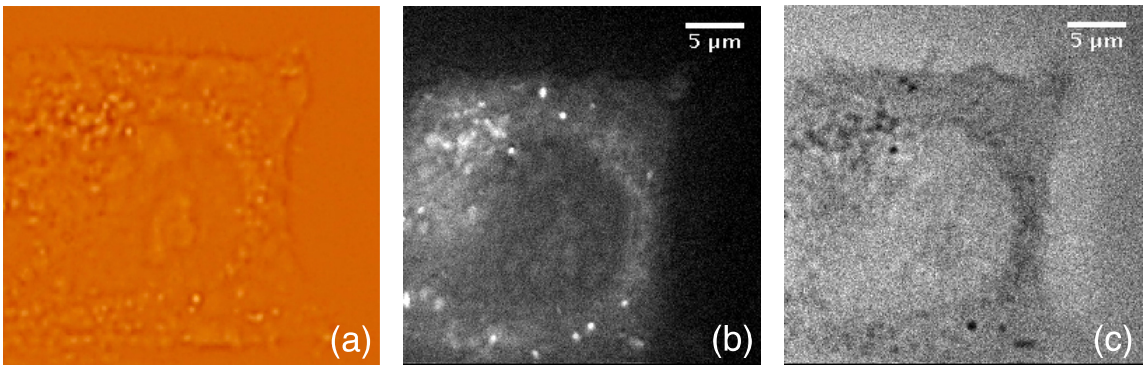

Fig. 3. (a) Brightfield microscopy, (b) on-resonance CARS and(c) off-resonance CARS images of a HuH7 cell in absence of MPIOs labels. Grayscale values vary from 3 to 60 in (b) and from 6 to 20 in (c)

3.3. Imaging of HuH7 cells incubated with MPIOs

The localization of MPIOs in cells was investigated after incubating the HuH7 cells with a 1mL solution of iron oxide particles at a concentration of 10^7 particles/mL and 1mL growth medium. The low concentration ensured that a limited number of particles were taken up by the cell. We note that the use of MPIO solutions with higher concentration imposes no additional complications to the imaging process. Figure 4a shows the *on-resonance* CARS image of a 30 × 30 μm^2 region depicting an isolated cell of elongated shape. The outside membrane of the cell is visible, as well as the contour of the nucleus. The image was collected from a focal plane near the center of the cell. The very large, circularly shaped nucleus can be identified by the lack of C-H signal, indicating lipids-rich aggregates are not present. The nucleus region presents uniform signal with intensity comparable to the surrounding aqueous

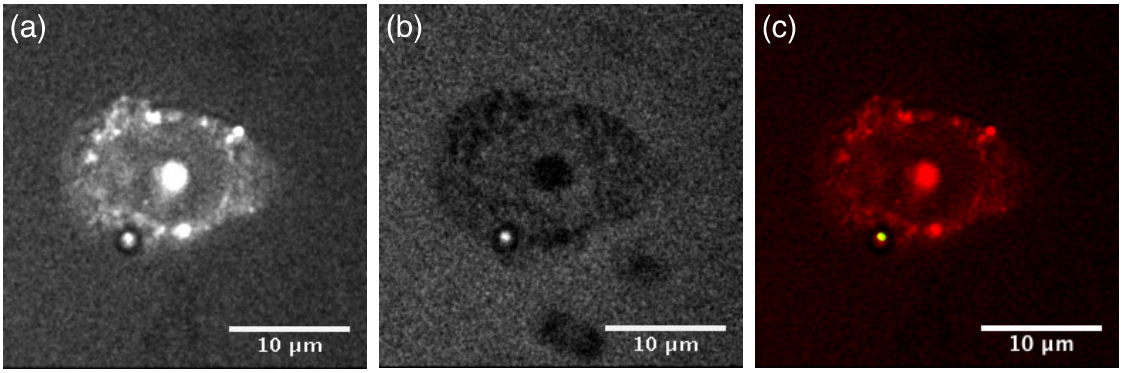

Fig. 4. (a) On-resonance and (b) off-resonance CARS images of a HuH7 cell incubated with MPIO solution. (c) is the overlay of the on- and off-resonance images where the former appears in red, and the background corrected off-resonance response appears in green. Grayscale values vary from 3 to 40 in (a) and from 3 to 25 in (b). The overlay image obtained from on and off-resonance measurements allows identification of a single iron oxide particle in the lower part of the cell (green spot).

#150798 - $15.00 USD Received 8 Jul 2011; revised 25 Jul 2011; accepted 28 Jul 2011; published 29 Jul 2011

growth medium. As shown previously in Ref. [55], the bright region inside the nucleus can be identified as the nucleolus, containing high densities of proteins and nucleic acids generating intense CARS signals. Several round features with a diameter of ~1 μm can be identified inside the cytoplasm. The challenge of our imaging approach is exemplified by this image; are we able to resolve which of the features in Fig. 4a are MPIOs and distinguish them from lipid-rich cell components? The CARS response in Fig. 4b shows that only one such features also presents a high intensity also in the *off-resonance* image of the cell, indicating the presence of an iron oxide particle. All other cellular features appear in the negative-like fashion similar to that in Fig. 3c; the cell is still visible with negative contrast relative to the water background. In this case also the nucleolus is visible as a dark region in the center of the nucleus.

Visual inspection already reveals that the bright feature in the *off-resonance* image finds immediate correspondence in the *on-resonance* image. This observation is confirmed by the color-coded overlay of the two images presented in Fig. 4c, where the *on-* and *off-resonance* images were added after subtraction of the background in Fig. 4b, where the background is defined as the average value of the intensity of the signal collected from the medium surrounding the cell. The *on-resonance* image of the cell appears in red, superimposed with the MPIO signature obtained from the *off-resonance* image in green. The identification of the particle is here unambiguous despite the many morphologically similar lipid droplets present in the cell, and we have obtained a label-free and non-invasive fast image of the intracellular distribution of MPIOs. The particle has been internalized by the cell, and is located within the cytoplasm in the proximity of the cellular membrane in an axial plane that contains as well the nucleus and the nucleolus located ~2 μm above the surface of the glass support.

We can infer, *a posteriori*, that one feature of the MPIO allows a first-hand identification already in the *on-resonance* image, as the high intensity spot where the particle is located is surrounded by a dark halo. This effect is due to the large refractive index mismatch between the particle and the surrounding medium, resulting in a distortion of the beams foci that alters the CARS response at the interface [56]. This effect is instead not present in the brightfield images of cells incubated with MPIOs.

3.4. Three-dimensional intracellular localization of MPIOs

The optical sectioning capabilities of CARS are best exploited in three-dimensional images of the cell. Such 3D-images allow direct inspection of the spatial distribution of MPIOs within the cells. The brightfield microscopy image shown in Fig. 5a shows a projection of a cell with the nucleus located to the left and a collection of circular features are visible to the right in the cell, some of them presenting a diameter in the order of 1 μm. Again, it is not straightforward to distinguish MPIOs from lipid bodies in the image and from the optical image no information is available on the vertical position of the different structures relative to the upper and lower boundaries of the cell. In fact, inspection of Fig. 5a does not allow one to conclude that particles have been internalized by the cell, rather than being located at the outside of the membrane. Figures 5b-f are a sequence of overlays of *on-resonance* (red) and *off-resonance* (green) CARS images of the cell taken at descending vertical positions separated by 1 μm. The full outline of the cell can be observed. In Fig. 5f the interface between the cell and the underlying glass support is imaged. From Figs. 5c-d we conclude that the nucleus as well as the collection of lipid droplets on the right side of the cell are both located in the mid-sections of the cell. The colocalization with the non-resonant image also allows the identification of the volume distribution of MPIOs, which is particularly important in order to determine whether the internalization process has been successful. Two particles can be observed, the leftmost of which located in the upper region of the cell (see Figs. 5b-d) and the rightmost in the lower region of the cell closer to the glass substrate (see Figs. 5c-e). Hence, from this 3-dimensional CARS image we can conclude with certainty that two particles have been successfully internalized, appearing with a maximum signal at locations 2 μm (lower right particle, Fig. 5d) and 3 μm (upper left particle, Fig. 5c) above the glass support. The signature

#150798 - $15.00 USD Received 8 Jul 2011; revised 25 Jul 2011; accepted 28 Jul 2011; published 29 Jul 2011

of the particles clearly extends beyond their physical dimensions, as the axial resolution is larger (~1 μm) than the lateral resolution (~0.3 nm). The slight discrepancy between the location of the MPIOs in the *on-* and *off-resonance* images is most likely due to a slight relocation of the particles between the two measurement series. We can rule out the possibility that the change in position is due to optical tweezing by noting that this effect is not present in the combination of single layer images where the time interval between consecutive measurements is shorter. The set of *on/off resonance* CARS images provides unambiguous insight into the presence and three dimensional distribution of single MPIOs, granting access to information that is otherwise impossible to obtain from the brightfield image in Fig. 5a.

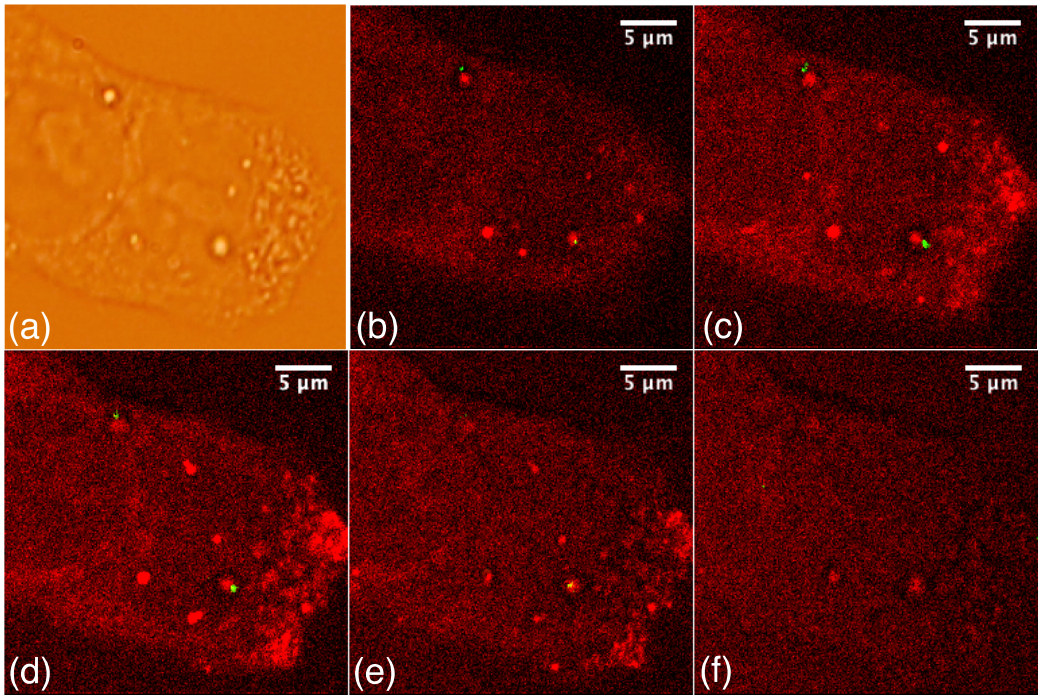

Fig. 5. (a) Brightfield microscopy image of a HuH7 cell incubated with MPIOs. (b-f) Overlay of on-resonance (red) and off-resonance (green) CARS images of the same cell with descending axial position (separated by 1 μm). Two internalized iron oxide particles (green) can be identified from the overlay images.

These results demonstrate that CARS microscopy enables objective verification of the particle uptake in living cells. This is of particular interest, since the particles and lipid droplets present similar morphology under brightfield microscopy, making the evaluation of their uptake dependent on the experience of the investigator. Moreover, the access to the exact intracellular localization of incorporated particles enables investigations of the interactions between particles and cell organelles, paving the way for long-term toxicity studies of importance from a clinical perspective.

4. Conclusion

We have shown that CARS microscopy is a suitable tool for intracellular visualization of micrometer-sized iron oxide particles and has the potential to become an important instrument for the development of tracers for cell tracking in clinical MRI. Compared to other techniques available for this purpose, CARS has the advantage of being a label-free non-invasive technique that gives sufficient contrast both for the visualization of the particles and the cellular environment without need of additional labels.

#150798 - $15.00 USD Received 8 Jul 2011; revised 25 Jul 2011; accepted 28 Jul 2011; published 29 Jul 2011

As magnetite is a small bandgap semiconductor, the four-wave mixing response of the particle does not benefit from additional enhancement of two-photon electronic excitation when the excitation beams are tuned to match the lipid CH stretches used for achieving contrast from the cellular body, hence the particles are not unambiguously identifiable from the *on-resonance* image of the cell alone. However, as non-resonant CARS is almost frequency-invariant, MPIOs are easily distinguished in the *off-resonance* image of the system. Overlays of the *on-* and *off-resonant* measurements enable the visualization of the position of the particles in the cells with sub-micron accuracy.

The immediate advantages of the use of CARS for this task are the chemical specificity that allows us to distinguish unambiguously the MPIOs from intracellular lipid-bodies of comparable dimensions, as well as the intrinsic three-dimensional imaging capabilities that allows us to identify the axial position of the particles in the cell with high precision.

The issues that CARS microscopy is capable of addressing are fundamental questions that naturally arise in the development stages of engineered particles, where physical properties of the particles are modified and additional surface functionalizations are added, modifying the interaction between the particles and the cell at the molecular level. Besides quantitative assessment of the efficacy of the internalization, additional information on the exact intracellular position of the MPIOs in comparison with other cell components are readily available in three-dimensions. It is easy to imagine scenarios where this information is particularly relevant if, e.g. nucleus penetration is desirable.

As an important outlook, we note that the CARS approach allows for following the kinetics of the particle uptake in real-time. Moreover, other subcellular components can be selectively visualized in CARS by probing molecular vibrations characteristic for e.g. mitochondria or nucleic acids [47], allowing the co-localization of the particles with other cell components with high specificity and without labeling. Also, CARS measurements can readily be combined with two-photon fluorescence (2PF) on most CARS setups. Hence, using markers for specific internalization processes and combining CARS and 2PF, information on the process responsible for the uptake of the particles can be obtained.

Acknowledgments

The authors gratefully acknowledge M.Sc. Lena Nyberg for providing the tripalmitin CARS spectrum of Fig. 1d. This study was financially supported by the Swedish Research Council (CB, AE), the European Regional Development Fund (EFRE 101443429) (CML, NR, IMS, MTM), the Nederlandse Organisatie voor Wetenschappelijk Onderzoek (Netherlands Organization for the Advancement of Research) (MB, JPRD, KFD, GR) and the COST action MP0603 microCARS (GR).